Internal optical forces in plasmonic nanostructures

T. V. Raziman and Olivier J. F. Martin*

Nanophotonics and Metrology Laboratory, Swiss Federal Institute of Technology (EPFL), Lausanne, CH-1015, Switzerland

*olivier.martin@epfl.ch

Abstract: We present a computational study of the internal optical forces arising in plasmonic gap antennas, dolmen structures and split rings. We find that very strong internal forces perpendicular to the propagation direction appear in these systems. These internal forces show a rich behaviour with varying wavelength, incident polarisation and geometrical parameters, which we explain in terms of the polarisation charges induced on the structures. Various interesting and anomalous features arise such as lateral force reversal, optical pulling force, and circular polarisation-induced forces and torques along directions symmetry-forbidden for orthogonal linear polarisations. Understanding these effects and mastering internal forces in plasmonic nanostructures will be instrumental in implementing new functionalities in these nanophotonic systems.

OCIS codes: (350.4855) Optical tweezers or optical manipulation; (240.6680) Surface plasmons; (250.5403) Plasmonics.

References and links

1. J. D. Jackson, *Classical Electrodynamics*, 3rd ed. (Wiley, 1998).
2. M. Mansuripur, "Radiation pressure and the linear momentum of the electromagnetic field," Opt. Express **12**, 5375–5401 (2004).
3. A. Ashkin, J. M. Dziedzic, J. E. Bjorkholm, and S. Chu, "Observation of a single-beam gradient force optical trap for dielectric particles," Opt. Lett. **11**, 288–290 (1986).
4. J. Chen, J. Ng, Z. Lin, and C. T. Chan, "Optical pulling force," Nat. Photonics **5**, 531–534 (2011).
5. A. Ashkin, "Acceleration and trapping of particles by radiation pressure," Phys. Rev. Lett. **24**, 156–159 (1970).
6. D. G. Grier, "A revolution in optical manipulation," Nature **424**, 810–816 (2003).
7. K. C. Neuman and S. M. Block, "Optical trapping," Rev. Sci. Instrum. **75**, 2787–2809 (2004).
8. J. R. Moffitt, Y. R. Chemla, S. B. Smith, and C. Bustamante, "Recent advances in optical tweezers," Annu. Rev. Biochem. **77**, 205–228 (2008).
9. H. Xu and M. Käll, "Surface-plasmon-enhanced optical forces in silver nanoaggregates," Phys. Rev. Lett. **89**, 246802 (2002).
10. M. Righini, A. S. Zelenina, C. Girard, and R. Quidant, "Parallel and selective trapping in a patterned plasmonic landscape," Nat. Phys. **3**, 477–480 (2007).
11. K. C. Toussaint, M. Liu, M. Pelton, J. Pesic, M. J. Guffey, P. Guyot-Sionnest, and N. F. Scherer, "Plasmon resonance-based optical trapping of single and multiple Au nanoparticles," Opt. Express **15**, 12017–12029 (2007).
12. R. Quidant and C. Girard, "Surface-plasmon-based optical manipulation," Laser Photon. Rev. **2**, 47–57 (2008).
13. L. Huang, S. J. Maerkl, and O. J. F. Martin, "Integration of plasmonic trapping in a microfluidic environment," Opt. Express **17**, 6018–6024 (2009).
14. M. L. Juan, M. Righini, and R. Quidant, "Plasmon nano-optical tweezers," Nat. Photonics **5**, 349–356 (2011).
15. V. D. Miljković, T. Pakizeh, B. Sepulveda, P. Johansson, and M. Käll, "Optical forces in plasmonic nanoparticle dimers," J. Phys. Chem. C **114**, 7472–7479 (2010).
16. R. Zhao, P. Tassin, T. Koschny, and C. M. Soukoulis, "Optical forces in nanowire pairs and metamaterials," Opt. Express **18**, 25665–25676 (2010).

#242743 Received 11 Jun 2015; revised 17 Jul 2015; accepted 22 Jul 2015; published 24 Jul 2015

17. Q. Zhang, J. J. Xiao, X. M. Zhang, Y. Yao, and H. Liu, "Reversal of optical binding force by fano resonance in plasmonic nanorod heterodimer," Opt. Express **21**, 6601–6608 (2013).
18. Q. Zhang and J. J. Xiao, "Multiple reversals of optical binding force in plasmonic disk-ring nanostructures with dipole-multipole fano resonances," Opt. Lett. **38**, 4240–4243 (2013).
19. A. Ji, T. V. Raziman, J. Butet, R. P. Sharma, and O. J. F. Martin, "Optical forces and torques on realistic plasmonic nanostructures: a surface integral approach," Opt. Lett. **39**, 4699–4702 (2014).
20. P. Mühlschlegel, H.-J. Eisler, O. J. F. Martin, B. Hecht, and D. W. Pohl, "Resonant optical antennas," Science **308**, 1607–1609 (2005).
21. M. Righini, P. Ghenuche, S. Cherukulappurath, V. Myroshnychenko, F. J. Garca de Abajo, and R. Quidant, "Nano-optical trapping of Rayleigh particles and *Escherichia coli* bacteria with resonant optical antennas," Nano Lett. **9**, 3387–3391 (2009).
22. W. Zhang, L. Huang, C. Santschi, and O. J. F. Martin, "Trapping and sensing 10 nm metal nanoparticles using plasmonic dipole antennas," Nano Lett. **10**, 1006–1011 (2010).
23. B. Gallinet and O. J. F. Martin, "Influence of electromagnetic interactions on the line shape of plasmonic fano resonances," ACS Nano **5**, 8999–9008 (2011).
24. A. Lovera and O. J. F. Martin, "Plasmonic trapping with realistic dipole nanoantennas: Analysis of the detection limit," Appl. Phys. Lett. **99**, 151104 (2011).
25. S. Zhang, D. A. Genov, Y. Wang, M. Liu, and X. Zhang, "Plasmon-induced transparency in metamaterials," Phys. Rev. Lett. **101**, 047401 (2008).
26. N. Verellen, Y. Sonnefraud, H. Sobhani, F. Hao, V. V. Moshchalkov, P. V. Dorpe, P. Nordlander, and S. A. Maier, "Fano resonances in individual coherent plasmonic nanocavities," Nano Lett. **9**, 1663–1667 (2009).
27. B. Luk'yanchuk, N. I. Zheludev, S. A. Maier, N. J. Halas, P. Nordlander, H. Giessen, and C. T. Chong, "The Fano resonance in plasmonic nanostructures and metamaterials," Nat. Mater. **9**, 707–715 (2010).
28. J. Pendry, A. Holden, D. Robbins, and W. Stewart, "Magnetism from conductors and enhanced nonlinear phenomena," IEEE Trans. Microw. Theory Tech. **47**, 2075–2084 (1999).
29. D. R. Smith, W. J. Padilla, D. C. Vier, S. C. Nemat-Nasser, and S. Schultz, "Composite medium with simultaneously negative permeability and permittivity," Phys. Rev. Lett. **84**, 4184–4187 (2000).
30. P. Gay-Balmaz and O. J. F. Martin, "Efficient isotropic magnetic resonators," Appl. Phys. Lett. **81**, 939–941 (2002).
31. A. M. Kern and O. J. F. Martin, "Surface integral formulation for 3D simulations of plasmonic and high permittivity nanostructures," J. Opt. Soc. Am. A **26**, 732–740 (2009).
32. M. Nieto-Vesperinas, P. C. Chaumet, and A. Rahmani, "Near-field photonic forces," Phil. Trans. R. Soc. Lond. A **362**, 719–738 (2004).
33. M. Ploschner, M. Mazilu, T. F. Krauss, and K. Dholakia, "Optical forces near a nanoantenna," J. Nanophoton. **4**, 041570 (2010).
34. J.-W. Liaw, W.-J. Lo, and M.-K. Kuo, "Wavelength-dependent longitudinal polarizability of gold nanorod on optical torques," Opt. Express **22**, 10858–10867 (2014).
35. F. Abelès, "Surface electromagnetic waves ellipsometry," Surf. Sci. **56**, 237–251 (1976).
36. A. N. Grigorenko, P. I. Nikitin, and A. V. Kabashin, "Phase jumps and interferometric surface plasmon resonance imaging," Appl. Phys. Lett. **75**, 3917–3919 (1999).
37. Y. S. Joe, A. M. Satanin, and C. S. Kim, "Classical analogy of Fano resonances," Phys. Scr. **74**, 259–266 (2006).
38. T. V. Raziman and O. J. F. Martin, "Polarisation charges and scattering behaviour of realistically rounded plasmonic nanostructures," Opt. Express **21**, 21500–21507 (2013).
39. T. V. Raziman, R. J. Wolke, and O. J. F. Martin, "Optical forces in nanoplasmonic systems: how do they work, what can they be useful for?" Faraday Discuss. **178**, 421–434 (2015).
40. L. Tong, V. D. Miljković, and M. Käll, "Alignment, rotation, and spinning of single plasmonic nanoparticles and nanowires using polarization dependent optical forces," Nano Lett. **10**, 268–273 (2010).
41. R. A. Beth, "Mechanical detection and measurement of the angular momentum of light," Phys. Rev. **50**, 115–125 (1936).
42. L. Allen, M. W. Beijersbergen, R. J. C. Spreeuw, and J. P. Woerdman, "Orbital angular momentum of light and the transformation of Laguerre-Gaussian laser modes," Phys. Rev. A **45**, 8185–8189 (1992).
43. H. He, M. E. J. Friese, N. R. Heckenberg, and H. Rubinsztein-Dunlop, "Direct observation of transfer of angular momentum to absorptive particles from a laser beam with a phase singularity," Phys. Rev. Lett. **75**, 826–829 (1995).
44. A. T. O'Neil, I. MacVicar, L. Allen, and M. J. Padgett, "Intrinsic and extrinsic nature of the orbital angular momentum of a light beam," Phys. Rev. Lett. **88**, 053601 (2002).
45. P. B. Johnson and R. W. Christy, "Optical constants of the noble metals," Phys. Rev. B **6**, 4370–4379 (1972).
46. B. Gallinet and O. J. F. Martin, "Relation between near–field and far–field properties of plasmonic fano resonances," Opt. Express **19**, 22167–22175 (2011).
47. Z. Li, S. Zhang, L. Tong, P. Wang, B. Dong, and H. Xu, "Ultrasensitive size-selection of plasmonic nanoparticles by fano interference optical force," ACS Nano **8**, 701–708 (2014).
48. H. Chen, S. Liu, J. Zi, and Z. Lin, "Fano resonance-induced negative optical scattering force on plasmonic

#242743 Received 11 Jun 2015; revised 17 Jul 2015; accepted 22 Jul 2015; published 24 Jul 2015

nanoparticles," ACS Nano **9**, 1926–1935 (2015).
49. H. Guo, N. Liu, L. Fu, T. P. Meyrath, T. Zentgraf, H. Schweizer, and H. Giessen, "Resonance hybridization in double split-ring resonator metamaterials," Opt. Express **15**, 12095–12101 (2007).
50. L. Huang and O. J. F. Martin, "Reversal of the optical force in a plasmonic trap," Opt. Lett. **33**, 3001–3003 (2008).
51. A. Potts, D. M. Bagnall, and N. I. Zheludev, "A new model of geometric chirality for two-dimensional continuous media and planar meta-materials," J. Opt. A: Pure. Appl. Opt. **6**, 193 (2004).
52. A. Lehmuskero, R. Ogier, T. Gschneidtner, P. Johansson, and M. Käll, "Ultrafast spinning of gold nanoparticles in water using circularly polarized light," Nano Lett. **13**, 3129–3134 (2013).
53. J. Chen, J. Ng, K. Ding, K. H. Fung, Z. Lin, and C. T. Chan, "Negative optical torque," Sci. Rep. **4**, 6386 (2014).
54. O. Vazquez-Mena, T. Sannomiya, M. Tosun, L. G. Villanueva, V. Savu, J. Voros, and J. Brugger, "High-resolution resistless nanopatterning on polymer and flexible substrates for plasmonic biosensing using stencil masks," ACS Nano **6**, 5474–5481 (2012).
55. X. Shen, T. J. Cui, D. Martin-Cano, and F. J. Garcia-Vidal, "Conformal surface plasmons propagating on ultrathin and flexible films," Proc. Natl. Acad. Sci. U.S.A. **110**, 40–45 (2013).
56. P. Guo, D. Sikdar, X. Huang, K. J. Si, B. Su, Y. Chen, W. Xiong, L. W. Yap, M. Premaratne, and W. Cheng, "Large-scale self-assembly and stretch-induced plasmonic properties of coreshell metal nanoparticle superlattice sheets," J. Phys. Chem. C **118**, 26816–26824 (2014).
57. S. J. Tan, M. J. Campolongo, D. Luo, and W. Cheng, "Building plasmonic nanostructures with DNA," Nat. Nanotechnol. **6**, 268–276 (2011).
58. X. Shen, A. Asenjo-Garcia, Q. Liu, Q. Jiang, F. J. Garca de Abajo, N. Liu, and B. Ding, "Three-dimensional plasmonic chiral tetramers assembled by DNA origami," Nano Lett. **13**, 2128–2133 (2013).
59. N. Li, A. Tittl, S. Yue, H. Giessen, C. Song, B. Ding, and N. Liu, "DNA-assembled bimetallic plasmonic nanosensors," Light Sci. Appl. **3**, e226 (2014).

1. Introduction

Propagating light waves contain momentum, which they can impart to particles [1, 2]. The more common and intuitive scenario is that of light pushing the particles in the direction of propagation, the so-called scattering force [3]. However, it is also possible to pull particles by certain optical beams [4]. In addition, inhomogeneities in the electric field intensity intrinsic to the incident beam or created due to the presence of other structures interacting with the incident field can result in a gradient force on the particle as well [3]. Such optical forces have been used for trapping and manipulating particles since the pioneering work of Ashkin [5], and have found practical applications in areas of physical and life sciences [6–8]. Plasmonic nanostructures facilitate optical manipulation at the nanoscale by providing high field intensities and gradients [9–14].

Theoretical studies of plasmonic optical tweezers with propagating waves concern themselves primarily with forces in the direction of or opposite to the wave propagation. However, the presence of plasmonic nanostructures can lead to the particles experiencing a lateral force perpendicular to the direction of propagation of the incident wave as well, as seen, for example, in nanoparticle dimers [15]. Obviously, internal forces will also arise within a nanostructure upon illumination, especially when this nanostructure is composed of several parts. However, to the best of our knowledge, such internal forces have never been studied except in some dimer systems [15–19]. In this article, we computationally investigate the internal forces on the individual parts of three compound systems commonly encountered in plasmonics : the plasmonic gap antenna, the dolmen structure, and the split ring resonator. Gap antennas were one of the first plasmonic structures providing high field enhancement with easy tunability, and have been utilised for optical trapping as well [20–24]. The dolmen system has also been of considerable interest in plasmonics since it supports a Fano resonance due to the coupling between the dipolar mode in the horizontal arm and the quadrupolar mode supported by the vertical arms [25–27]. Split ring resonators have been used as building blocks for metamaterials, and have permitted the creation of effective media with interesting physical properties such as negative refraction [28–30]. Studying the internal forces in these representative and ubiquitous

#242743 Received 11 Jun 2015; revised 17 Jul 2015; accepted 22 Jul 2015; published 24 Jul 2015

plasmonic systems will help to understand how internal forces arise generally in plasmonic systems.

The electromagnetic response of the nanostructures is simulated using the surface integral equation (SIE) formulation [31]. The plasmonic structures are modelled with the background medium as vacuum. The optical forces and torques on the particles are computed using the Maxwell's stress tensor method [1, 32–34]:

$$\mathbf{F} = \oint_S \sigma \cdot \mathbf{n} \, \mathrm{dS}, \text{ and} \tag{1}$$

$$\mathbf{T} = \oint_S \mathbf{r} \times \sigma \cdot \mathbf{n} \, \mathrm{dS}, \tag{2}$$

where $\mathbf{F}$ and $\mathbf{T}$ are the optical force and torque on the structure under investigation, respectively. S is a closed surface enclosing the structure, and $\mathbf{r}$ is a point on the surface with area element dS and unit outward surface normal vector $\mathbf{n}$. σ is the time-averaged Maxwell's stress tensor given by

$$\sigma = \frac{1}{2}\Re[\varepsilon \mathbf{E}\mathbf{E}^* + \mu \mathbf{H}\mathbf{H}^* - \frac{1}{2}(\varepsilon \mathbf{E}\cdot\mathbf{E}^* + \mu \mathbf{H}\cdot\mathbf{H}^*)\mathbf{I}], \tag{3}$$

where $\mathbf{E}$ and $\mathbf{H}$ are the complex electric and magnetic total fields, and ε and μ are the permittivity and permeability of the background medium, respectively. $\Re$ denotes the real part, and the asterisk denotes complex conjugation. The stress tensor integration is performed directly over the discretised particle surface using surface electric and magnetic currents for improved speed and accuracy [19]. Surface polarisation charges (q) were calculated from the discontinuity in the normal component of electric field at the surfaces, as

$$q = \varepsilon_0(\mathbf{E}_{out} - \mathbf{E}_{in}) \cdot \mathbf{n}. \tag{4}$$

The charge computation was done directly from the surface currents in the same manner as the forces and torques. The scattering cross section (C_{sc}) of the structures was evaluated by integrating the flux of the scattered Poynting vector over a sphere of radius 50 μm around the structure and normalising it to the incident field intensity,

$$C_{sc} = \frac{\oint_S \frac{1}{2} Re\,[\mathbf{E}_{sc} \times \mathbf{H}_{sc}^*] \cdot \mathbf{n} \, \mathrm{dS}}{\left|\frac{1}{2} Re\,[\mathbf{E}_{in} \times \mathbf{H}_{in}^*]\right|}. \tag{5}$$

2. Results and discussion

2.1. Gap antenna

We first look at the simplest of the three systems, the plasmonic gap antenna. The gap antenna we study is symmetric with arm lengths of 600 nm and has a circular cross section with radius 20 nm. The gap size is 20 nm, and the faces of the antenna are fully rounded. The arms are made of Drude metal with the permittivity defined by

$$\varepsilon(\omega) = \varepsilon_\infty - \frac{\omega_p^2}{\omega(\omega + i\gamma)}, \tag{6}$$

with the parameters $\varepsilon_\infty = 9.1$, $\omega_p = 9.0843$ eV and $\gamma = 0.07078$ eV. The system is illuminated by a plane wave polarised along the axis of the antenna (x-axis) and propagating in the z-direction, as depicted in the schematic in the inset of Fig. 1(a).

#242743 Received 11 Jun 2015; revised 17 Jul 2015; accepted 22 Jul 2015; published 24 Jul 2015

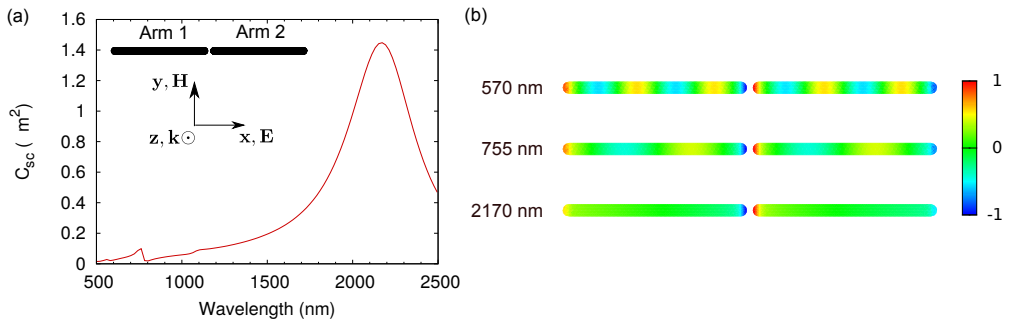

Fig. 1. (a) Scattering cross section as a function of wavelength for a symmetric gap antenna with arm lengths of 600 nm and gap size of 20 nm, shown in inset. (b) Normalised polarisation charges induced on the antenna arms at selected wavelengths.

The scattering cross section C_{sc} of the antenna is shown in Fig. 1(a). The dipolar resonance is visible at 2170 nm, with higher order scattering peaks present at 755 nm and 570 nm. The polarisation charges induced on the structure at these three wavelengths are shown in Fig. 1(b). The induced dipole moment shows a transition from being in phase with the incident light to being out of phase across each plasmon resonance, similar to classical driven oscillators [35–37]. At the resonance, the dipole moment and hence the charges are 90 degrees out of phase with the incident field. As a result, the imaginary part of the complex polarisation charges dominates over the real part, and is what is plotted in Fig. 1(b). The charge distributions are independently normalised to the maximum charge density at each wavelength. The charge plots clearly depict the higher order nature of the low-wavelength peaks. In all cases, the charge concentration is very high at the gap-faces of both arms [38,39]. The charge distribution shows an odd symmetry about the gap centre, resulting in opposite charges being created at the gap faces of the two arms, suggesting an attractive force between the arms in all cases.

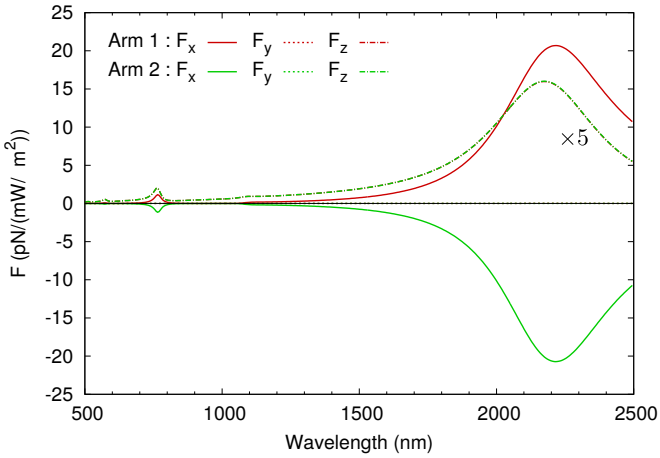

Fig. 2. Optical forces on the symmetric antenna arms. Different force components along x-, y- and z-directions are considered (see axes in the inset of Fig. 1(a)).

Indeed, the force on the arms plotted in Fig. 2 validates this. The force between the two arms in the x-direction is always attractive, and equal in magnitude as symmetry dictates. Also, the attractive force F_x is very strong due to the large concentration of charges across the small gap,

#242743 Received 11 Jun 2015; revised 17 Jul 2015; accepted 22 Jul 2015; published 24 Jul 2015

nearly an order of magnitude stronger than the scattering force F_z at the same wavelength. For a wide wavelength range, the lateral force trumps the scattering force in magnitude. Also note that the force along the y-axis is zero, as expected from symmetry considerations. Typical trapping experiments have a laser power of approximately 50 mW, focused to a spot of about 5 μm. The intensity felt by the illuminated plasmonic structure is thus nearly 1 mW/μm^2, resulting in a lateral force as strong as 20 pN, which is very high for a nano-object.

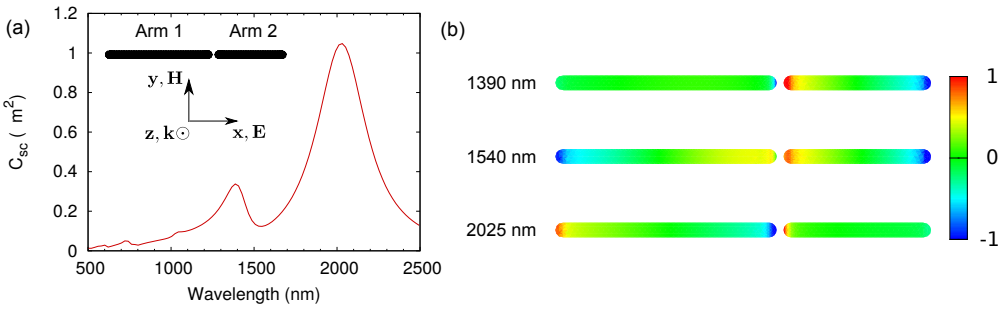

Fig. 3. (a) Scattering cross section as a function of wavelength for an asymmetric gap antenna with arm lengths of 600 nm and 400 nm, and gap size of 20 nm, shown in inset. (b) Normalised polarisation charges induced on the antenna arms at selected wavelengths.

We now repeat the calculations for an asymmetric nanoantenna. The geometry is same as earlier in all respects, except that the right arm is now shorter, measuring 400 nm, as shown in the inset of Fig. 3(a). The scattering cross section for this geometry is plotted in Fig. 3(a). We note that the dipolar peak has split into two, each peak corresponding to the excitation of one of the arms as is evident from the charge distribution at the two peaks plotted in Fig. 3(b). Note that the imaginary part of the charges are plotted at the scattering peaks due to the same reason as earlier, whereas real part of the charges are plotted at the dip since it is dominant away from the resonances. The plots for each wavelength are normalised independently to the maximum charge density at the wavelength. At the lower wavelength peak, the shorter arm is excited, which in turn induces opposite charges at the gap face of the longer arm. At the higher wavelength peak, it is the longer arm which is excited and induces opposite charges on the longer arm. At both these wavelengths, we would expect the force between the arms to be attractive.

However, at the scattering dip between the two peaks, we see something different. Both arms are now individually excited by the incident light directly, and since we are at either side of the resonance of the two arms, the dipole moments of the two arms are aligned in opposite directions. As a result, the charges on the two sides of the gap now have the same sign, and we expect a repulsive force between the arms, a situation completely unlike the symmetric case.

The forces on the system are plotted in Fig. 4. Similar to the case of the symmetric antenna, the lateral force F_x on either arm is higher than the scattering force F_z for much of the wavelength range. It is seen that at both scattering peaks, the arms attract each other strongly. However, at an intermediate range, the force becomes repulsive as expected from the charge distribution. The change of force from attractive to repulsive between the two scattering peaks of an asymmetric nanoantenna has been previously reported by Zhang *et al.* [17].

The behaviour of the scattering force itself is interesting. First of all, the forces on the two arms in the z-direction are no longer equal since the symmetry has been broken. The magnitude of the scattering force on the arm undergoing resonant excitation is higher than that of the other arm at both scattering peaks. More interestingly, at the shorter arm resonance, the longer arm is pulled towards the incident field rather than being pushed away by it, resulting in an optical

#242743 Received 11 Jun 2015; revised 17 Jul 2015; accepted 22 Jul 2015; published 24 Jul 2015

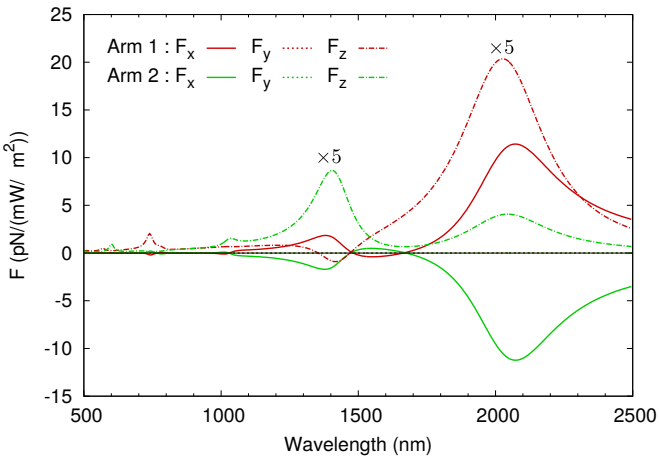

Fig. 4. Optical forces on the asymmetric antenna arm.

pulling force.

The torque about the centre of mass of the system in the y-direction is plotted in Fig. 5. This figure shows the contrast between the scattering forces acting on the two arms more clearly, since the y-component of the torque arises from the variation in the z-component of force in this case. For the symmetric antenna, there would have been no y-torque. Instead, what we see here is a significant magnitude of torque – that is, the lever arm is comparable to the size of the antenna. The sign of the torque also depends on the wavelength. Had the antenna been a rigid system, the shorter arm would have ended up aligning in the direction of the incident field or opposite to it depending on the wavelength of incidence. This behaviour thus offers the possibility of optically orienting nanoparticles. Note that we are talking about wavelength-dependent alignment in the direction of propagation here, as opposed to alignment in the direction of polarisation using polarisation dependent optical forces [34, 40].

Though light can possess both spin and orbital momentum and impart them to particles just

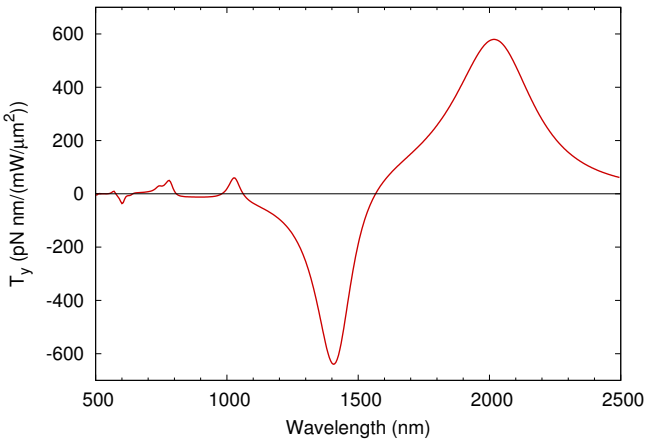

Fig. 5. y-component of the optical torque about the centre of mass of the asymmetric antenna.

#242743 Received 11 Jun 2015; revised 17 Jul 2015; accepted 22 Jul 2015; published 24 Jul 2015

as in the case of linear momentum, plane waves do not possess orbital angular momentum, and linearly polarised waves do not possess spin angular momentum either [1, 41–44]. In spite of this, the linearly polarised plane wave is able to transfer angular momentum to the gap antenna due to the asymmetry.

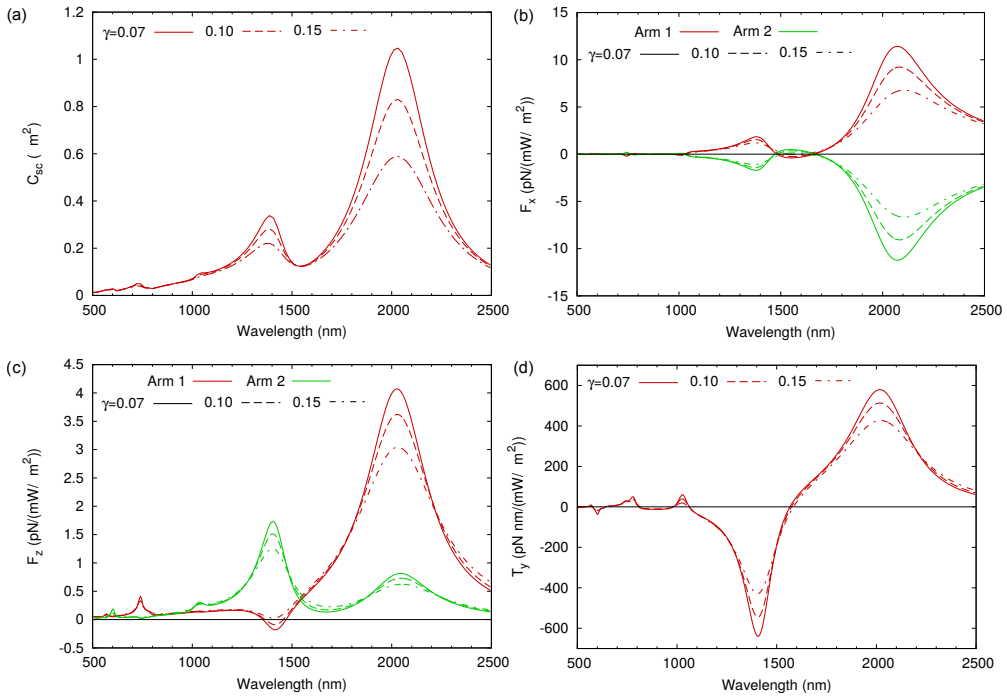

Fig. 6. (a) Scattering cross section, (b) x-component of force, (c) z-component of force, and (d) y-component of torque on the asymmetric antenna as a function of wavelength for various values of the loss parameter γ in Eq. (6).

Finally, we look at the dependence of the forces and torque on the losses in the system. The asymmetric nanoantenna is simulated with two further values of loss parameter γ in Eq. (6), $\gamma = 0.10$ and $\gamma = 0.15$, leaving other material and geometric parameters the same. The change in scattering cross section of the system on varying the loss parameter is plotted in Fig. 6(a). The scattering peaks become weaker in intensity and broader in wavelength with increasing values of loss. Apart from this, all the qualitative features of the scattering curve are retained since the imaginary part of the permittivity is still much smaller than the real part in the wavelength range of interest. The x- and z-components of force on the arms plotted in Figs. 6(b) and 6(c) and the y-component of torque on the system plotted in Fig. 6(d) also show only changes in magnitude with varying loss parameter. The magnitude changes are the highest near the scattering peaks where the scattering cross section shows the highest variation since the forces and torques on the system are directly correlated to the scattering cross section and dipole moment induced on the structure. However, all the qualitative features discussed previously are retained.

2.2. *Dolmen structure*

We now move on to analyse the internal forces on a more complicated system, the dolmen. The dolmen structure we study here consists of a horizontal arm of length 120 nm and two vertical arms of length 110 nm. All three have cross sections of 40 nm $\times$ 40 nm, and the faces are rounded to a radius of 10 nm. The dolmen is made of gold, with permittivity data taken

#242743 Received 11 Jun 2015; revised 17 Jul 2015; accepted 22 Jul 2015; published 24 Jul 2015

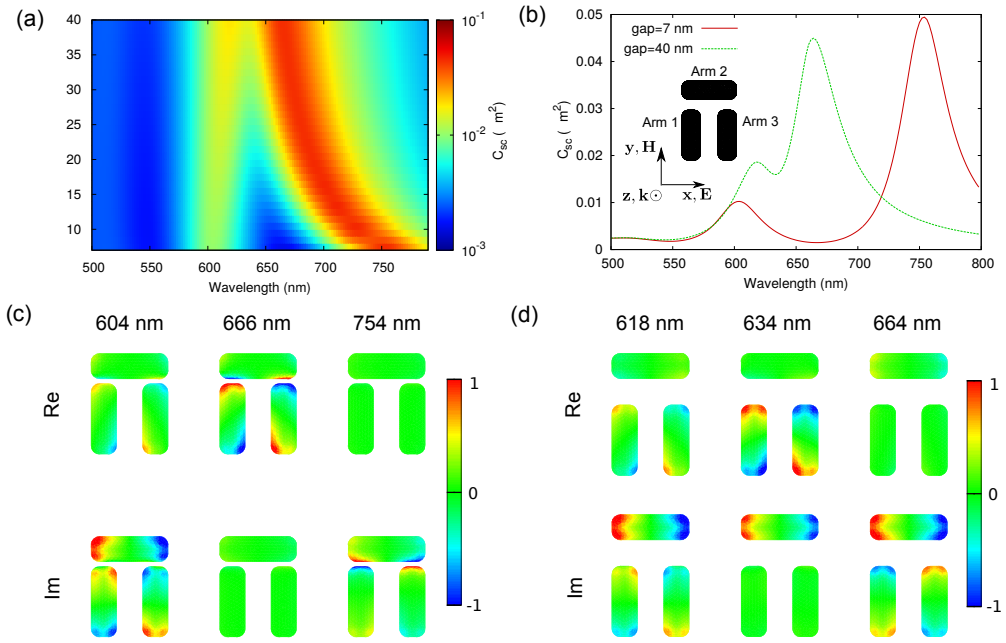

Fig. 7. (a) Scattering cross section as a function of wavelength and vertical gap size for the dolmen structure. (b) Scattering cross section of the dolmen for two representative vertical gap sizes, 7 nm and 40 nm. Geometry depicted in inset. (c) Real and imaginary parts of the induced polarisation charges for a dolmen with 7 nm vertical gap at the two scattering peak wavelengths and the scattering dip wavelength. (d) Same as (c) for a vertical gap of 40 nm.

from Johnson and Christy [45]. The dolmen is illuminated by a plane wave propagating in the z-direction and polarised along the x-direction, as depicted in the inset of Fig. 7(b).

The scattering cross section as a function of wavelength and the gap between the horizontal and vertical arms of the dolmen is plotted in Fig. 7(a). We see two scattering peaks which increase in separation as the gap is reduced increasing the coupling between the horizontal and vertical arms. For clarity, the scattering cross sections for two extreme values of the gap (7 nm and 40 nm) are shown in Fig. 7(b). The scattering dip is the signature of the Fano resonance [46]. Fano resonances are known to play a crucial role in determining the forces on asymmetric systems and in inhomogeneous fields [17, 18, 47, 48].

The normalised polarisation charge distributions at the two scattering peaks and the dip for 7 nm gap are shown in Fig. 7(c), and the same for 40 nm gap in Fig. 7(d). Since the polarisation charges induced on the different arms of the dolmen show different phase relationships with the incident field at the relevant wavelengths unlike the case of the gap antenna, both the real and imaginary parts of the polarisation charges have been shown. The real part of the charges can be understood as the charges present at time $t = 0$, whereas the imaginary part corresponds to the charges present at $t = T/4$, where T is the time period of the incident wave. Note that the real and imaginary plots for each wavelength are normalised together to the highest value of change density in the two plots.

For both gaps, the lower wavelength peak corresponds to the anti-bonding mode. The charges induced on the gap-faces of the horizontal and vertical arms are of the same sign, and they clearly repel each other, forcing the charges to move away from the gap. On the other hand, at the higher wavelength peak, we have the bonding mode being excited and the charges on either side of the gap are opposite in sign and attract each other towards the gap. In these scenarios,

#242743 Received 11 Jun 2015; revised 17 Jul 2015; accepted 22 Jul 2015; published 24 Jul 2015

we expect repulsive and attractive forces, respectively. The charges created on the horizontal arm are weaker at the Fano dip – more so in the case of strong coupling (small gap) than weak coupling (large gap) – whereas the charges on the vertical arms are still significant.

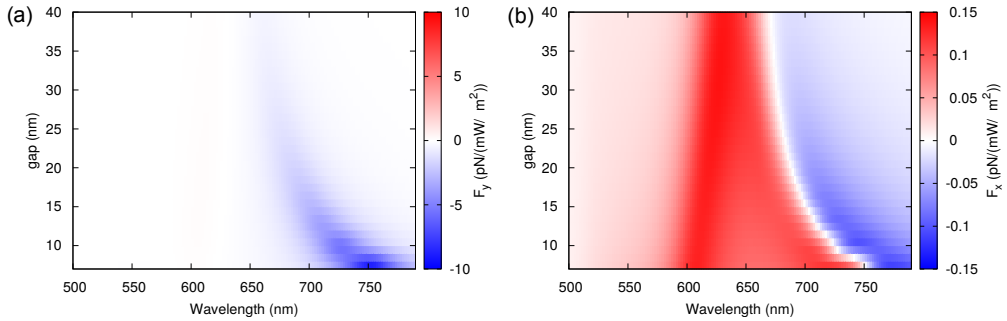

Fig. 8. Optical forces on (a) horizontal arm (arm 2) of the dolmen along y-direction, and (b) left vertical arm (arm 1) along x-direction.

The y-component of the force on the horizontal arm (arm 2) as a function of wavelength and the gap size is shown in Fig. 8(a). The major feature is the band where the arm is strongly attracted to the vertical arms (negative force in y direction). This follows the higher wavelength peak in scattering quite well. In addition, there is a band where it is very weakly repelled (positive force in y-direction), which follows the lower wavelength peak in scattering. Both these features can be well-explained by the charge distributions in the two cases, as described earlier. The relative weakness of the repulsive force compared to the attractive force is a result of the lower dipole moment at the anti-bonding mode, which is also evident from the scattering cross section at the two peaks.

The x-component of the force on the left vertical arm (arm 1) as a function of the same parameters is shown in Fig. 8(b). Clearly, this component of the force is much weaker than the y-component. This should not be unexpected since there is no pair of closely separated charges across a gap here unlike in the y direction. What would seem surprising is that for large wavelengths, the force in the x-direction is repulsive between the vertical arms. If we had considered the x-force to be arising purely from the interaction between anti-parallel dipoles separated by a distance much shorter than the wavelength, we would have expected an attractive force throughout the wavelength range. However, these arms are extended dipoles, and the charges on the horizontal arm play a role in the x-component of the force as well. For short wavelengths, the charges at the gap faces of the horizontal and vertical arms have the same sign. This means that the top part of the vertical arm is subject to attractive forces both from the top part of the other vertical arm and the far end of the horizontal arm. These attractive forces would be stronger than the repulsion from the like charges at the bottom part of the opposite arm due to the higher separation for this pair. As a result, the net force is attractive. However, once we move to the higher wavelength regime, the charge distribution at the far end of the horizontal arm will start to repel the charges at the top of the horizontal arm. This eventually takes over since the dipole moment of the horizontal arm is stronger than that of the vertical arms as it is fed directly by the incident field. As expected, this transition from attractive to repulsive x-force happens around the higher wavelength scattering peak, as can be seen from comparing Fig. 7(a) and Fig. 8(b).

For clarity, the forces on the arms for a gap of 7 nm are shown in Fig. 9(a) and the same for a gap of 40 nm in Fig. 9(b). The attractive lateral force in the y-direction is an order of magnitude stronger than the scattering force in the z-direction for the shorter gap. Even the lateral force in

#242743 Received 11 Jun 2015; revised 17 Jul 2015; accepted 22 Jul 2015; published 24 Jul 2015

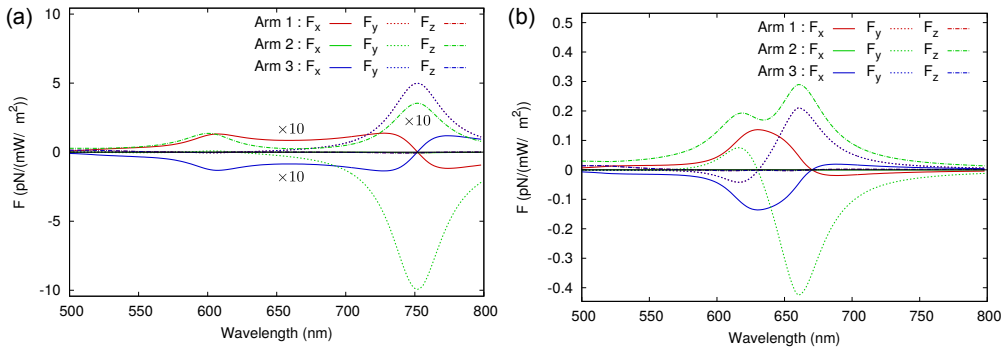

Fig. 9. Optical forces on the arms of the dolmen for vertical gap size of (a) 7 nm, and (b) 40 nm.

the x-direction is comparable to the scattering force for most of the wavelength range. Note that the scattering force is significant only on the horizontal arm for longer wavelengths since the horizontal dipole is what is directly excited by the incident field and scatters into the far field. For the larger gap, the y-forces are significantly reduced as a result of the increased charge separation. However, the y-component of the force on the horizontal arm is still the strongest force in the system, being stronger than the scattering force F_z. All the non-zero components of the lateral forces have the same order of magnitude as the scattering force.

2.3. Split-ring resonator

Finally, we look at the lateral forces in a split ring resonator. The structure we study here is formed out of two concentric rings lying in the xy plane with 10 nm gaps on each ring. The outer ring has a radius of 140 nm whereas the inner ring has a radius of 80 nm, with both rings having a cross sectional radius of 20 nm. The rings are aligned such that centres of the gaps on both rings lie on the x-axis. All gap faces are fully rounded. The rings are made of Drude metal with frequency-dependent permittivity following Eq. (6), with Drude parameters $\varepsilon_\infty = 9.5$, $\omega_p = 8.95$ eV and $\gamma = 0.0691$ eV. The structure is illuminated by a plane wave propagating in the z-direction.

It is instructive to see the response of the two rings individually first, since the optical response of the split ring can be understood in terms of hybridisation of the modes of individual rings [49]. Figure 10(a) shows the scattering response of the inner ring as a function of wavelength for linear polarisations along x- and y-axes, and two circular polarisations L and R with opposite senses of rotation. There is a single scattering peak for polarisation along x-axis, whereas there are two peaks for polarisation along y-axis in the wavelength range considered. The response for the circular polarisations is just a combination of the two linear polarisations. The imaginary parts of the polarisation charges induced for the three peaks is shown in Fig. 10(b). The peaks for y-polarisation at 1880 nm and 725 nm are first and second order charge distributions along the circumference of the ring, with strong concentration of charges at the ends of the gap. On the other hand, the charge distribution for the x-polarisation peak at 865 nm is the dipolar charge distribution along x-direction.

In the same vein, Fig. 10(c) shows the scattering response of the outer ring. Once again, we have one scattering peak for x-polarisation and two for y-polarisation. However, there is one difference as seen from the charge distribution plots in Fig. 10(d). The charge distribution for the x-polarisation peak at 1320 nm is the dipolar distribution along the x direction. However, the y-polarisation peaks at 1050 nm and 720 nm show second and third order distributions along the circumference of the ring. This should not come as unexpected, since increasing the size of

#242743 Received 11 Jun 2015; revised 17 Jul 2015; accepted 22 Jul 2015; published 24 Jul 2015

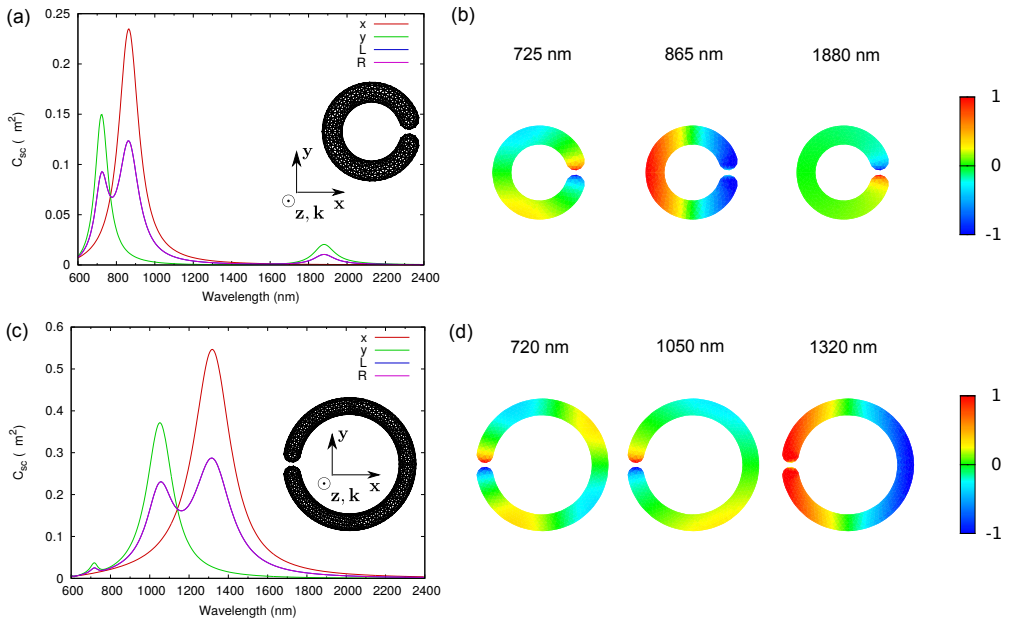

Fig. 10. (a) Scattering cross section for different incident polarisations for the inner ring in the split ring structure, as shown in inset. (b) Polarisation charges induced on the inner ring at the scattering peak wavelengths. (c) and (d) show the same results as in (a) and (b), respectively, for the outer ring.

the ring red shifts the scattering spectrum. As a result, the first order peak for the y-polarisation has red shifted outside the wavelength range considered here.

We can now look at the scattering response of the combined split ring system, shown in Fig. 11(a). There are two scattering peaks for x-polarised incident light and four for y-polarised incidence. The imaginary parts of the polarisation charge distributions for all six peaks are shown in Fig. 11(b). The charge distributions for the x-polarisation peaks at 880 nm and 1500 nm show them to be parallel and anti-parallel hybrids of the x-polarisation peaks of the inner and outer rings. The charge distribution at the isolated y-polarisation peak at 1925 nm essentially follows the inner ring-only charge distribution at 1880 nm whereas the peak at

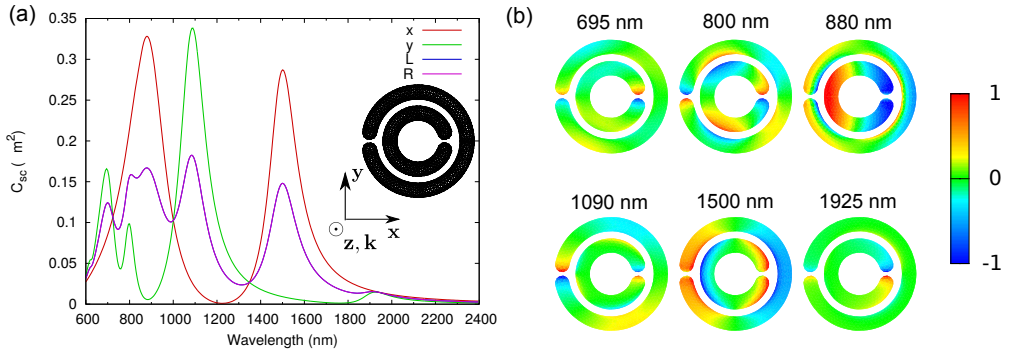

Fig. 11. (a) Scattering cross section for different incident polarisations, and (b) polarisation charges at the scattering peak wavelengths for the split ring structure.

#242743
Received 11 Jun 2015; revised 17 Jul 2015; accepted 22 Jul 2015; published 24 Jul 2015

1090 nm follows the outer ring-only distribution at 1050 nm. The peaks at 695 nm and 800 nm seem to be parallel and anti-parallel hybrids of the inner and outer ring charge distributions at 725 nm and 720 nm, respectively. That is, all scattering peaks of the combined system can be understood in terms of the responses of the individual rings.

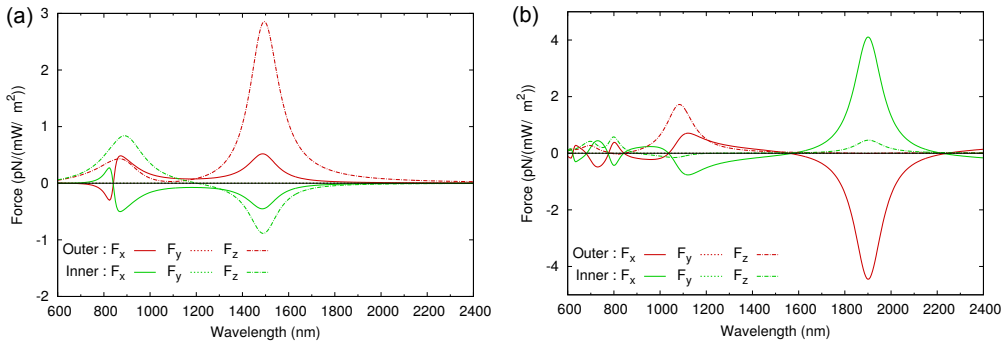

Fig. 12. Optical forces on the rings in the split ring structure for (a) x-, and (b) y-polarised incident field.

The forces on the two rings for x-polarised incident light are shown in Fig. 12(a). The scattering force in the z-direction is significantly stronger than the lateral force in x-direction. The y-component of the force is zero by symmetry. The direction of the x-component of the lateral force on the outer ring switches from left to right (and vice-versa for the inner ring), similar to the behaviour we had seen in the dolmen structure. Had the rings been gap-free, there would have been no lateral force in the x direction either. Hence the lateral forces are created by the small charge asymmetry introduced by the gap, which is what makes the lateral forces weak. Due to the near-dipolar nature of the charge distributions for x-polarisation, it is difficult to qualitatively explain the origin of the switch merely using the polarisation charges like we did earlier. Once again, as in the case of the asymmetric antenna, we have a situation where the inner ring is pulled by the incident plane-wave rather than being pushed away from it.

The forces for y-polarised incidence are plotted in Fig. 12(b). Unlike the previous case, the lateral forces in the x-direction are comparable or larger than the scattering force in the z-direction. This is because the charge asymmetry is higher since the charges are strongly concentrated at the gaps. At 1925 nm where the inner gap is excited strongly, it induces polarisation charges on the nearby regions of the outer ring, resulting in the inner ring being pushed to the right and the outer ring to the left. At 1090 nm where the outer gap is excited, the situation is reversed. Once again, symmetry ensures that there is no lateral force in the y-direction.

It is interesting to compare the forces observed here with those found in the disk-ring Fano system by Zhang and Xiao [18]. In that system, the authors had uncovered the existence of force reversals and explained them in terms of the hybridization between the dipole modes of the disk and the multipole modes of the ring. There are a few factors which make the two systems very different. First of all, the disk and the ring were placed side-by-side instead of concentrically as the rings here . As a result, the coupling between the modes of the system happened entirely across the small gap between the disk and the ring - on the contrary, the hybrid modes of the split ring show coupling throughout the length of the rings as is evident from the charge distribution. Also, the charge concentration at the ring gaps and the resulting strong attractive force near the gap were features absent in the disk-ring system. These features make the description of forces in the split ring system more complicated. However, the basic feature that the energy of the hybridised modes dictates the force reversals is retained, which has been observed in systems as simple as a particle in a trap [50].

#242743 Received 11 Jun 2015; revised 17 Jul 2015; accepted 22 Jul 2015; published 24 Jul 2015

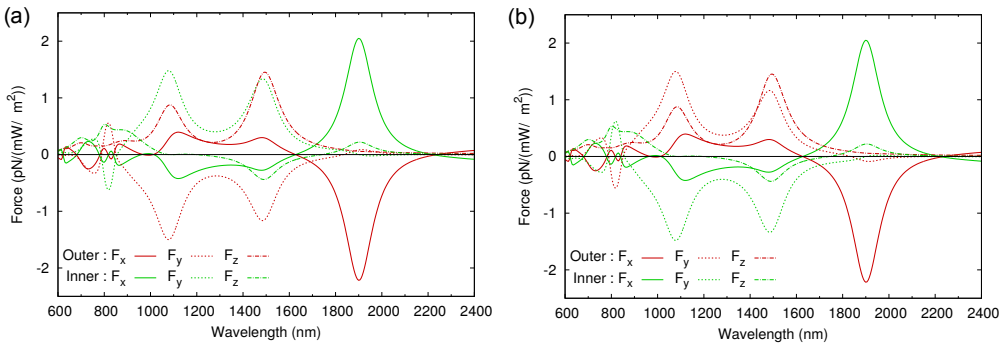

Fig. 13. Optical forces on the rings in the split ring structure for (a) L-, and (b) R-polarised incident field.

Figures 13(a) and 13(b) show the forces for L- and R-polarised incidence, respectively. Surprisingly, we see that the y-component of the force is not zero anymore in spite of the inversion symmetry of the structure about y- axis. In fact, it is the strongest force in the problem for much of the wavelength range. The reason for this apparent geometrical symmetry violation is that the force operator is not linear on the incident fields. Though the incident and scattered fields for circular polarised incidence can be expressed as a linear combination of the fields for x- and y-polarised incidence, the same is not true for the forces as there are cross-terms. It is probably most intuitive to understand the origin of this force component in terms of polarisation charges. When the incident light is x-polarised, the induced charge distribution is even about the x-axis. On the other hand, when the incident light is y-polarised, the charge distribution is odd. Both odd and even symmetries result in a zero net force in the y-direction. However, if we take an arbitrary linear combination of x-and y polarisations, which is what happens in the case of circular polarisation, the induced charge distribution is neither odd nor even about the x-axis, and we cannot expect zero net force anymore. The importance of circular polarisation in the origin of y-force can be seen from the fact that the sign of the y-force switches on switching the sense of rotation of light, whereas the other components of force do not change. We would like to stress that the y-force is not a result of the chirality of the structure. The split ring structure has both xy and xz planes as mirror symmetry planes, so that the chirality of the structure is zero even if we consider two dimensional chirality [51].

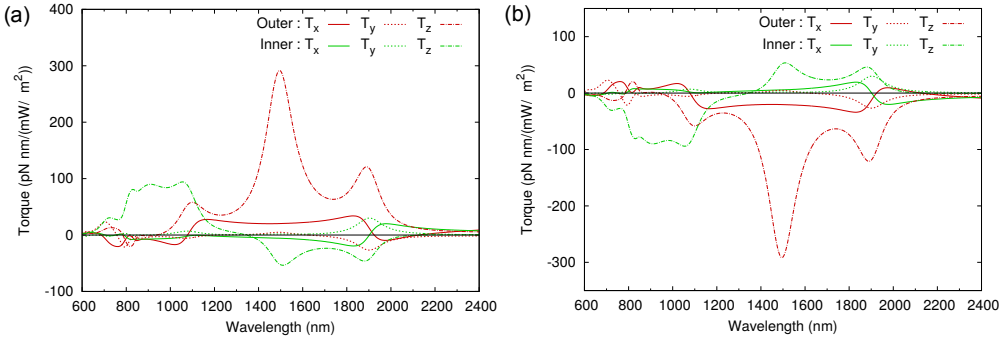

Fig. 14. Optical torques on the rings in the split ring structure for (a) L-, and (b) R-polarised incident field.

Finally, we look at the torque on the two rings produced by L and R polarised light, as

#242743 Received 11 Jun 2015; revised 17 Jul 2015; accepted 22 Jul 2015; published 24 Jul 2015

shown in Figs. 14(a) and 14(b). We see a behaviour exactly opposite to the force in that, on switching the sense of rotation of the light, only y-torque remains unchanged whereas the other components switch sign. This should not be surprising since the y-component of the force affects the x-and z- components of torque. In particular, the x-component of the torque arises in the same fashion as the y-component of force, and would have been symmetry-forbidden for x- and y-polarisations.

What is more interesting is that the sense of rotation imparted to the ring need not be the same as that of the incident light. It is intuitive to understand particles absorbing circularly polarised photons and rotating in the same sense as the incoming light [52]. This can be considered analogous to the scattering forces which push the particle in the direction of wave propagation. However, there exists the phenomenon of negative optical torque, the analogue of optical pulling forces, where the particle ends up rotating in the opposite sense of the angular momentum of incident light [53]. We see such behaviour in the z-component of the torque on the inner ring. We see two distinct wavelength regimes where the z-torque imparted has opposite signs, meaning that the ring can end up rotating in the opposite sense of the angular momentum of the incoming photons.

As a final remark, we would like to add that though the simulations have been performed with vacuum as the background medium, the qualitative behaviour is expected to be retained in other backgrounds. The anomalous features uncovered here such as force reversal and negative optical torques will be present in other media where optical trapping and tweezing experiments are performed in, though there will be associated wavelength shifts and changes in force magnitudes. Fabricating the plasmonic systems on soft substrates which can be deformed by the optical forces should enable the experimental verification of these numerical results [54–56]. Though the presence of substrates can change the optical response of the nanostructures, the differences in optical forces and torques can be minimized by performing the experiments in a fluid which is index-matched to the substrate. The mechanical stresses induced on the substrate will also have to be taken into account. Another possibility would be to perform experiments on self-assembled complex nanoplasmonic systems which provide significant freedom of motion [57–59].

3. Conclusion

We have shown that in the different plasmonic systems considered here, internal forces are significant, and even become stronger than the scattering force in the system in many cases. Internal forces between particles can be qualitatively understood in terms of the polarisation charges induced by the incident light. These lateral forces show a rich behaviour, switching between regimes of attraction and repulsion depending on wavelength and inter-particle distance. The nonlinear nature of the force operator results in an interesting dependence on polarisation as well, creating forces in apparently geometrically symmetry-forbidden directions. Keeping all these in mind, lateral forces should be analysed properly along with the scattering/trapping forces while designing trapping experiments since the lateral forces could play a major role in directing the particles to be trapped towards or away from the trapping sites. We have also shown strong optical torques arising in these systems as a result of the lateral forces and also the appearance of negative optical torque, which could be utilised for optical orientation of nanoparticles.

Acknowledgments

The authors would like to thank R. J. Wolke for help with generating the simulation meshes. Funding from the Swiss National Science Foundation (Project 200020_135452) is gratefully acknowledged.

#242743 Received 11 Jun 2015; revised 17 Jul 2015; accepted 22 Jul 2015; published 24 Jul 2015